

Hybrid LES/RANS Calculation of High Speed Jet Noise

Xiaodan Cai* and Foluso Ladeinde†
TTC Technologies, Inc., P.O. Box 1527, Stony Brook, NY 11790

Ramons A. Reba‡ and Robert H. Schlinker§
United Technologies Research Center, E. Hartford, CT 06108 USA

This paper presents near-field and far-field LES results from a hybrid RANS/LES simulation of two high-speed jets at $M_\infty=0.9$ ($T_j/T_\infty=0.86$: Tanna's Set Point 7 (SP7) and $T_j/T_\infty=2.7$: Tanna's Set Point 46 (SP46)).¹⁷ The near-field pressure is analyzed in terms of hydrodynamic wave-packets (Reba et al.¹⁰) to quantify the large scale turbulence noise source. Results indicate that the simulation reasonably captures the spatio-temporal evolution of the large-scale turbulence. However, the LES-predicted turbulence structures appear to be significantly more energetic, with a consistent over-prediction of 10 dB in the near-field pressure. The acoustic far field is computed using a Ffowcs-Williams/Hawkings surface. Acoustic results show good qualitative agreement with the experimental data. The predicted far field OASPL directivity pattern compares well with the experiments, despite an over-prediction of 3 dB and 10 dB for SP7 and SP46, respectively.

I. Introduction

THE noise from a high-speed jet engine during take-off and landing poses a serious environmental concern to military bases. Modeling of the jet noise can facilitate early evaluation of environmental impact and enable analysis of technology and methods to control it.

In recent years, jet noise modeling research has largely followed two complementary paths: (1) the acoustic analogy approach, wherein RANS-computed turbulence length scales and kinetic energy are used to parameterize ad-hoc or empirical models for acoustic source statistics, and (2) Large Eddy Simulation (LES), where the largest turbulence scales and their sound generation are computed directly. The former approach has proven successful in predicting noise from fine-scale turbulence, which dominates the noise signature at 90 degrees to the jet axis, but has thus far been unsuccessful in predicting noise from large-scale turbulence, which controls peak radiation at aft angles.^{7,23,24} The LES approach, on the other hand, has been successful in predicting aft angle radiation at low to moderate frequencies ($St < 1$), but due to prohibitive computational expenses, the LES procedure is limited to simple round jets and low Reynolds number.^{2,3,4,5} The effects of complex nozzle geometry of engineering interest have not been addressed (Bogey and Bailly⁶). Therefore, there are concerns about the boundary conditions at the nozzle exit, which need to be resolved for accurate jet flow and noise prediction.

The hybrid LES/RANS approach proposed by Shur et al¹⁶ is examined in our studies with a focus on the performance of high-order numerical discretization schemes. The procedure includes two steps. During the first step, a coupled nozzle-jet 3D RANS computation is performed. Then, LES is carried out for the jet plume with the inflow conditions at the nozzle exit taken from the RANS solution in the first step. Shur et al¹⁶ argue that by doing so, no forcing parameters are needed to excite the shear layer. Instead, the nozzle lip provides the necessary receptivity location for generating and reflecting acoustic waves.

* Senior Research Engineer, AIAA Member.

† Director of Research, AIAA Lifetime Member and Associate Fellow

‡ Project Leader, Senior AIAA Member

§ Project Leader, Components, AIAA Associate Fellow

The near-field flows are post-processed using the Ffowcs-Williams/Hawkings surface-integration method to calculate the far-field sound. The predicted sound directivities are compared with experiments and previous numerical simulations by Bodony and Lele.¹⁸ In addition to the far field acoustics, we present comparisons in terms of the large scale turbulence source characteristics. This relies on a wave-packet framework (Reba et al.¹⁰), wherein the hydrodynamic pressure in the jet linear near-field region is viewed as the sound source. With this framework, the large-scale turbulence sound source can be measured experimentally with relative ease using microphones located in the jet near-field region just outside the non-linear turbulent flow. This concept was previously applied to heated and unheated subsonic jets (Reba et al.^{[10][11]}), with acoustic Mach numbers ranging from 0.5 to 1.33. Assessing the ability of our LES methodology to capture the large scale turbulence source characteristics is a key objective of the current study. This represents a critical validation step beyond far field comparisons, since fortuitous compensating errors in the near field can potentially lead to acceptable agreement in the far field.

Our calculations are based on a high-fidelity computational fluid dynamics (CFD) platform with high-order accurate numerical schemes implemented for all-speed flows (6th order compact scheme for subsonic flows and 5th order WENO scheme for shock-embedded flows).¹⁴ In the following, we first present the numerical procedures used in our simulations, followed by the hybrid LES/RANS strategy, a detailed description of grid resolution and its requirement and distribution, the boundary condition treatment, and finally hydrodynamic and acoustic results.

II. Numerical Procedure

The fully-compressible form of the continuity, momentum, and energy equations are solved in this study which, in a generalized curvilinear coordinate system, can be written as

$$\frac{\partial(Q/J)}{\partial t} + \frac{\partial\hat{F}}{\partial\xi} + \frac{\partial\hat{G}}{\partial\eta} + \frac{\partial\hat{H}}{\partial\zeta} = \frac{\partial\hat{F}_v}{\partial\xi} + \frac{\partial\hat{G}_v}{\partial\eta} + \frac{\partial\hat{H}_v}{\partial\zeta} + \hat{S}, \quad (1)$$

where Q is the vector of conserved variables, $Q = (\rho, \rho u, \rho v, \rho w, \rho E)^T$, $(\hat{F}, \hat{G}, \hat{H})$ are the convective fluxes, $(\hat{F}_v, \hat{G}_v, \hat{H}_v)$ are the viscous fluxes, and \hat{S} is the source term (this term is non-zero only in the energy equation). J is the Jacobian of the transformation between the generalized coordinate system (ξ, η, ζ) and physical coordinate system (x, y, z) .

The spatial schemes in our high-order procedures are based on the finite difference method, because of its low cost relative to other options such as finite volume and finite elements. Specifically, and as pointed out by Shu,¹² the finite volume method is approximately nine times as expensive, while finite elements could even be more expensive because of the numerical quadrature that will be necessary for high-order schemes. For low-order methods, we support the MUSCL-Roe schemes. We have implemented the compact and WENO schemes for high-order discretization. The compact scheme is intended for incompressible and subsonic flows, whereas WENO is used for high subsonic and supersonic flows. These schemes are summarized below in the form in which they are implemented in AEROFLOTM CFD package, which was used to generate the basic solutions in this study.

MUSCL-Roe

This simple, fairly robust, low-order scheme which uses Roe flux-splitting at the mid-point values was introduced by van Leer. First, the left and right values of the primitive variables at the mid-point between two nodes are computed as

$$\phi_{i+1/2,L} = \phi_i + \beta_i \quad (2)$$

and

$$\phi_{i+1/2,R} = \phi_{i+1} - \beta_{i+1} \quad (3)$$

where $\phi = (\rho, u, v, w, p)^T$ is the vector of primitive variables and β_i is the ‘‘limited slope’’ at point i . Here, p is the thermodynamic pressure. The limited slopes β_i are computed using van Leer’s harmonic limiter.

Based on the left and right states at $i+1/2$, the numerical flux is computed using Roe flux-splitting as

$$\hat{F}_{i+\frac{1}{2}} = \frac{1}{2} \left(\hat{F}_{i+\frac{1}{2},L} + \hat{F}_{i+\frac{1}{2},R} - |A| \left(\left(\frac{Q}{J} \right)_R - \left(\frac{Q}{J} \right)_L \right) \right). \quad (4)$$

Here, R and L values are constructed using the corresponding values of the primitive variables in Eqn. (1). Matrix $|A|$ is constructed based on the Roe-averaged state at $i+1/2$

$$|A| = R_{Roe} |\Lambda_{Roe}| R_{Roe}^{-1}, \quad (5)$$

where $|\Lambda|$ is the diagonal matrix of the absolute eigenvalues of the Jacobian, $\partial \hat{F} / \partial Q$.

COMPACT

The Padé method is used to approximate the spatial derivatives for subsonic flows. Consider the differencing of a variable ϕ (e.g. a conserved variable, a flux component) along the ξ direction, that is, $\phi' = \partial \phi / \partial \xi$. An implicit, centered finite difference formula is employed to calculate the numerical values ϕ'_i :

$$\alpha \phi'_{i-1} + \phi'_i + \alpha \phi'_{i+1} = b \frac{\phi_{i+2} - \phi_{i-2}}{4\Delta\xi} + a \frac{\phi_{i+1} - \phi_{i-1}}{2\Delta\xi}. \quad (6)$$

The parameters α , a , and b determine the spatial accuracy of the algorithm, and their values are determined using Taylor series expansions around point i . For a sixth-order accurate scheme,^{1,13} $(\alpha, a, b) = (1/3, 14/9, 1/9)$.

Compact finite differences are non-dissipative and are susceptible to numerical instabilities due to non-linear flow features. In order to enforce numerical stability, a low-pass filtering procedure is adopted. For a typical component of the solution vector, ϕ , the filtered values $\tilde{\phi}$ are obtained from

$$\alpha_f \tilde{\phi}_{i-1} + \tilde{\phi}_i + \alpha_f \tilde{\phi}_{i+1} = \sum_{k=0}^N \frac{a_k}{2} (\phi_{i+k} + \phi_{i-k}). \quad (7)$$

The coefficients a_k are expressed in terms of α_f .¹³ α_f controls the strength of the filter; as it is reduced, a wider band of high frequencies is damped. A range $0.3 \leq \alpha_f < 0.5$ is suggested.

WENO

For high-order differencing of flow fields with shock waves, the characteristic-wise weighted essentially non-oscillatory (WENO) procedure is used (see Ref. [7],[22]). This numerical approach is summarized below.

Considering the ξ -direction as an example, we have

$$\frac{\partial \hat{F}}{\partial \xi} \Big|_i = \frac{1}{\Delta\xi} \left\{ \left[\tilde{R}_{Roe} \cdot (\tilde{R}_{Roe}^{-1} \cdot \hat{F}) \right]_{i+\frac{1}{2}} - \left[\tilde{R}_{Roe} \cdot (\tilde{R}_{Roe}^{-1} \cdot \hat{F}) \right]_{i-\frac{1}{2}} \right\}, \quad (8)$$

where \tilde{R}_{Roe} is the matrix formed with the right eigenvectors of the Jacobian $\partial \hat{F} / \partial Q$, computed based on a Roe-averaged state at $i \pm 1/2$. For the characteristic-wise WENO, the reconstruction procedure is performed on the characteristic fields $\hat{F}_c = \tilde{R}_{Roe}^{-1} \cdot \hat{F}$ to obtain the values at $i+1/2$. The left and right states at the mid-points are obtained using the Lax-Friedrichs flux-splitting method or the Roe flux-difference splitting method. For the former,

$$\hat{F}_c^\pm = \frac{1}{2} (\hat{F}_c \pm \alpha q), \quad (9)$$

where α is the spectral radius of the Jacobian $\partial \hat{F} / \partial Q$. The characteristic-wise fluxes at the mid-points are reconstructed as

$$\begin{aligned} \hat{F}_{c,i+\frac{1}{2}}^+ &= \sum_{r=0}^{k-1} \omega_r F_{c,i+\frac{1}{2}}^{(r)+}, \quad \hat{F}_{c,i+\frac{1}{2}}^- = \sum_{r=0}^{k-1} \tilde{\omega}_r F_{c,i+\frac{1}{2}}^{(r)-}, \\ F_{c,i+\frac{1}{2}}^{(r)} &= \sum_{m=0}^{k-1} c_{rm} \hat{F}_{c,i-r+m}, \end{aligned} \quad (10)$$

where ω_r and $\tilde{\omega}_r$ are normalized weights based on smoothness indicators of the numerical fluxes and c_{rm} are the coefficients of Lagrange interpolation. Finally, the reconstructed characteristic fluxes are converted back to physical space, $\hat{F}_{i+\frac{1}{2}}^\pm = \tilde{R}_{Roe} \cdot \hat{F}_{c,i+\frac{1}{2}}^\pm$, and the numerical flux formed as

$$\hat{F}_{i+\frac{1}{2}} = \hat{F}_{i+\frac{1}{2}}^+ + \hat{F}_{i+\frac{1}{2}}^- \quad (11)$$

The viscous fluxes are discretized with explicit second-order finite differences when the MUSCL scheme is used for the convective fluxes, and when compact (sixth-order) or WENO (fifth-order) finite difference are used for the convective fluxes, the viscous fluxes are discretized with high-order finite differences.

III. Noise Prediction Models

Hybrid LES/RANS Procedure

As mentioned earlier in this paper, a two-step hybrid LES/RANS procedure is used to simulate the nozzle flow with the interior flow of the nozzle included in the RANS calculations. During the first step, a coupled nozzle-jet 3D RANS computation is performed. Then, LES is carried out for the jet plume with the inflow conditions at the nozzle exit taken from the RANS solution in the first step. Therefore, as pointed out earlier in this paper, no forcing parameters are needed to excite the shear layer of the jet flows.

The specific form of the inflow conditions used in the LES calculations depends on whether or not the inflow is subsonic or supersonic, where inflow is defined as the jet exit ($-1/2 \leq r \leq 1/2, x/D = 0$). For supersonic inflow, all the flow parameters are specified from the RANS solution. For subsonic inflow, the pressure is calculated from

$$\frac{\partial p}{\partial t} + (u - c) \frac{\partial p}{\partial x} = 0, \quad (12)$$

where p is the instantaneous (turbulence mean plus fluctuating) static pressure and other variables are directly specified from the RANS solution. Note that the calculated pressure from RANS is used in place of Eqn. (12) in some of the calculations. For $x/D < 0$ (i.e., upstream of the nozzle exit) and $|r/D| > 1/2$ (radially outside of the nozzle), we extend the computational domain upstream to $x/D = -10$ and zero values are specified for the velocities and density and pressure have the ambient values. The assumption here is that the location is too far upstream to be affected by the jet flow, say by entrainment.

Near-Field Modal Decomposition

The wave packet model proposed by Reba et al. (2005) is based on the near-field cross-spectral density

$$R_m(x_1, x_2, \omega) = \langle p_m(x_1, \omega) p_m^*(x_2, \omega) \rangle, \quad (13)$$

where $p_m(x, \omega)$ is the Fourier-transformed pressure corresponding to azimuthal mode number m and frequency ω at axial location x , and the angular brackets denote ensemble averaging. When $x_1 = x_2$ (the diagonal entries of R_m), Eqn. (13) represents the power spectral density (PSD) at a given axial location. The off-diagonal entries of R_m characterize the spatial correlation of the turbulence.

Acoustic Far-Field

The far-field acoustics is obtained by the Ffowcs-Williams/Hawkings projection method, which can be written as

$$p'(\bar{x}, t) = p'_r(\bar{x}, t) + p'_l(\bar{x}, t) + p'_q(\bar{x}, t), \quad (14)$$

where

$$4\pi p'_r(\vec{x}, t) = \frac{\partial}{\partial t} \int_S \left[\frac{\rho_0 U_n}{r|1-M_r|} \right]_{ret} dS, \quad (14a)$$

$$4\pi p'_L(\vec{x}, t) = \frac{1}{c_0} \frac{\partial}{\partial t} \int_S \left[\frac{L_r}{r|1-M_r|} \right]_{ret} dS + \int_S \left[\frac{L_r}{r^2|1-M_r|} \right]_{ret} dS \quad (14b)$$

and p'_Q is the quadrupole noise due to turbulent stresses, which could be neglected in the potential region. P'_T is the thickness noise and P'_L is the loading noise. c_0 is the ambient sound speed, S represents the FW-H integration surface and r is the distance from the sound source to the observation point. In Eqn. (14), the subscripts r and n indicate the component of vectors in the radial direction (\vec{r}) and the surface normal directions (\vec{n}), respectively. The subscript *ret* refers to the quantities in the brackets taken at the retarded time. In Eqns. (14a) and (14b), $U_n = U_i n_i$ and $L_r = L_i r_i$ with variables U_i and L_i are defined as

$$U_i = \left(1 - \frac{\rho}{\rho_0} \right) V_i + \frac{\rho u_i}{\rho_0}, \quad (15a)$$

$$L_i = P_{ij} \hat{n}_j + \rho u_i (u_n - V_n), \quad (15b)$$

where P_{ij} is the compressive stress tensor with the constant $p_0 \delta_{ij}$ subtracted, u_i is the flow velocity, V_i is the velocity of the control surface, and $M_r = \vec{V} \cdot \vec{x} / (c|\vec{x}|)$.

Under the far-field condition ($r = |\vec{x}| \gg 1$), Eqn. (14) combined with Eqns. 14(a) and 14(b) can be simplified into

$$4\pi |1-M_r| |\vec{x}| \cdot p'(\vec{x}, t) = p'_Q(\vec{x}, t) + \frac{x_j}{|\vec{x}| c_0} \frac{\partial}{\partial t} \int_S [p' n_j + \rho u_j (u_n - V_n)]_{ret} dS + \frac{\partial}{\partial t} \int_S [\rho_0 u_n + \rho' (u_n - V_n)]_{ret} dS, \quad (16)$$

where M_r and r are assumed constant, thus taken out of the integration, and the second term on RHS of Eqn. (14b) has been neglected. Furthermore, when the integration surface is located in the region with potential flows dominating, p'_Q in Eqn. (16) can be neglected.

IV. Results

There are several numerical details in our LES/RANS procedure. First, the MILES (Monotone Integrated Large Eddy Simulation) approach are used for the LES calculations, which means that sub-grid models were not explicitly developed. Shur et al.¹⁶ gave a rationale for such a choice. Second, we have adopted the simple yet robust technique developed by Visbal and Gaitonde¹³ to handle the far-field boundary conditions. This approach exploits the characteristics of the low-pass filter provided by the rapid mesh stretching in regions outside the domain of interest. The odd-even acoustic modes reflected at the grid-coarsening interface are then annihilated by the high-order numerical filter implemented in AEROFLO. Finally, the minimum mesh resolution is desired for a specific flow problem. For the current high subsonic jets, the temperature ratios are $T_j / T_\infty = 0.86$ (cold jet) and $T_j / T_\infty = 2.7$ (hot jet), respectively. The Reynolds number is $Re_d = \rho_j U_j D / \mu_j = 2.0 \times 10^5$ for both jets. In a typical RANS

calculation, the first grid point based on wall units should have a value in the neighborhood of $y^+ \approx 1$. According to circular pipe turbulent theory, we have the following form:

$$y^+ = \frac{yu^*}{\nu} = \frac{y}{D} \cdot 0.2812 \cdot \text{Re}_D^{7/8}. \quad (17)$$

In our initial setup, we set the first grid point at $\delta y_1 / D$ of 10^{-4} , which corresponds to $\delta y^+ \approx 1.2$ and is fine enough to resolve the turbulent wall layers. On the other hand, the mesh size in the radial direction for LES could be chosen to be much larger than that for the RANS calculation since the flow inside the nozzle is not included in the LES calculations. A tentative grid size of 0.005 ($\delta y_{\min} = 0.005$) is used in the present study.

There is also an issue related to the resolution of wave propagations. For a typical jet noise, the peak Strouhal number ($f_p D_j / U_j$) with a value of approximately 0.4, which gives a wave length $\frac{\lambda_p}{D} = \frac{C_\infty}{Df_p} = \frac{C_\infty}{U} \cdot \frac{1}{fD/U} = \frac{C_\infty}{C_j} \cdot 2.8 = 1.7$. For the sound at shallow angles, the typical Helmholtz number ($f_p D_j / a_\infty$) is around 0.2, which corresponds to a wave length of $\lambda_p / D_j = C_\infty / (D_j f_p) = 5$. Compared with the turbulent integral length scale, the peak sound wave imposes less grid requirement. (For an example, a typical turbulent integral length scale is $L_x / D_j \approx 0.75$ at the end of the potential zone for the current test case.) However, to alleviate the numerical errors associated with the finite-domain boundary effects, the simulation of acoustics requires a larger domain size. In our simulations, we adopt a domain size as big as $60D_j$ in the downstream direction and $30D_j$ in the radial direction. To justify this choice, consider the following factors: first, for supersonic jet flows, the sound generation (not propagation) zones usually extend as far as $15D_j$ downstream of the nozzle exit, and a typical LES domain size must be extended to $25-30D_j$ ($15+2*\lambda_p$). (Two-wavelengths are added for the sound wave to propagate freely in the potential flow regions.). Considering our use of mesh stretching to damp the wave reflections from the numerical boundaries, we choose the stream-wise domain size as $60D_j$. On the other hand, for the radius direction, a typical LES domain size extends to $10-15D_j$ ($1.5+2*\lambda_p$). For the same reason of damping the reflections from the numerical boundaries, we choose the radial domain size as $30D_j$.

As seen above, resolving the near-wall turbulent length scales imposes the most stringent grid resolution requirement for both the RANS and LES calculations. To cover the computational domain from a mesh size range of $\delta y_1 / D = 10^{-4}$ to 60, judicious mesh refinement is required for affordable total grid resolution. A mesh size of approximately 1.5 million (RANS) and 2 million (LES) points have been tested in our simulations. Our major requirement in this study is that the peak noise should be accurately predicted.

Table 1. The nodal points in each block of the computational grid of RANS and LES.

(a) Block Size for the RANS Mesh			(b) Block Size for the LES Mesh		
No.	Topology	Total Size	No.	Topology	Total Size
1	51×61×65	202,215	1	51×61×65	202,215
2	51×61×65	202,215	2	61×61×65	241,865
3	51×61×65	202,215	3	61×61×65	241,865
4	51×71×65	235,365	4	61×61×65	241,865
5	51×71×65	235,365	5	61×51×65	202,215
6	101×17×17	29,189	6	61×51×65	202,215
7	51×17×17	14,739	7	61×51×65	202,215
8	51×61×65	202,215	8	181×33×33	197,109

An eight-block mesh system is shown in Figure 1 for RANS (a, b) and LES (c, d). The size of each mesh block is listed in Table 1. Blocks 7 and 8 in RANS model the interior flow of the nozzle, which is absent in Figure 1(b).

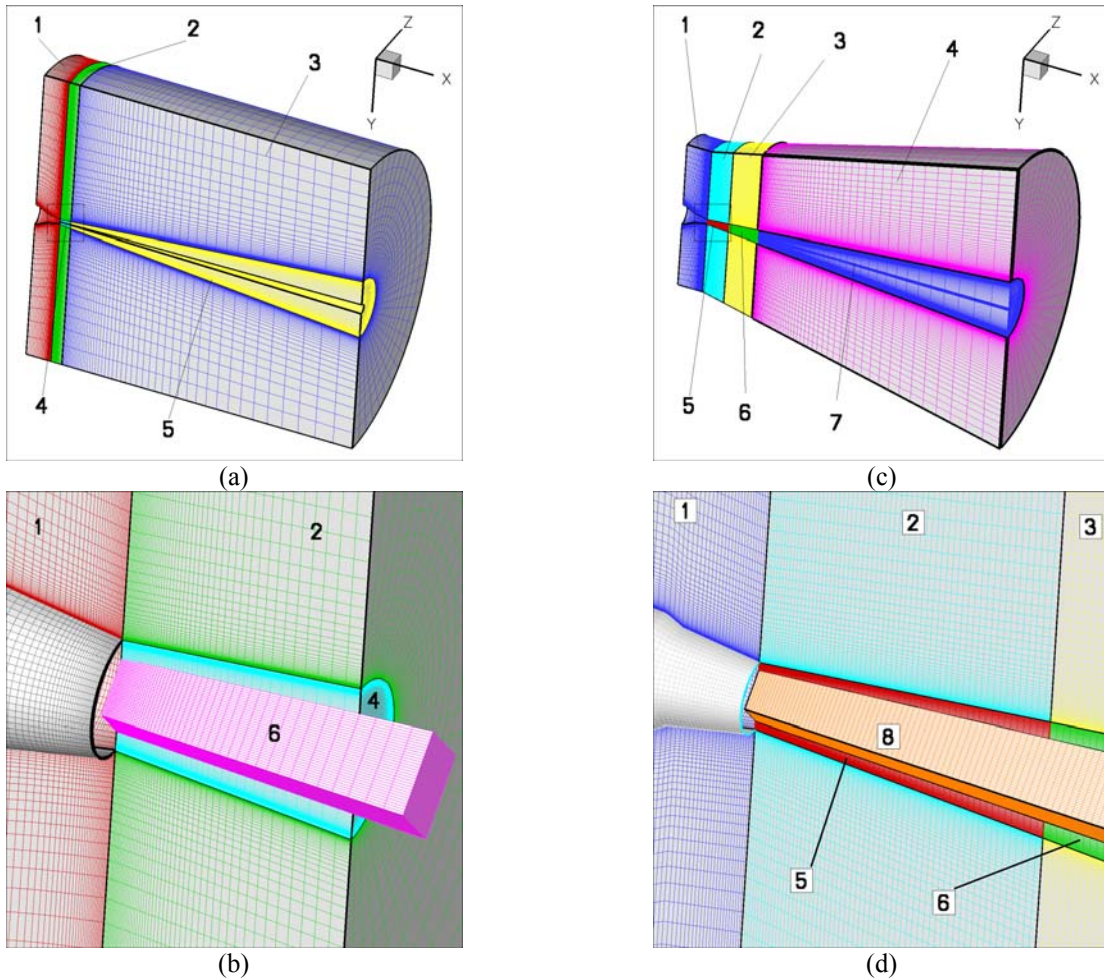


Figure 1. Multi-block computational mesh for RANS and LES calculations: a) Full view of the RANS mesh; b) Close-up view of the RANS mesh; c) Full view of the LES mesh; d) Close-up view of LES mesh.

A typical stream-wise velocity contour map of the converged RANS calculation of the hot jet is shown in Figure 2. Figure 3(a) shows the velocity profiles at the nozzle exit from the RANS calculations, which are normalized based on wall units. The velocity profile from both the hot and cold jets agree well with the near-wall Log-law profile, which demonstrates that the current RANS mesh may be fine enough to resolve the wall boundary layer flows inside the nozzle. The nozzle exit flow fields from the RANS calculations are then imposed as the inflow to the subsequent LES calculations. Compared to previous LES with artificially-imposed inflow conditions, such as the work of Bogey et al.³ and Bodony and Lele, the current inflow field at the nozzle exit plane has a much thinner boundary layer (Figure 3(b)). The Reynolds number and the momentum thickness of the inflow fields in our LES calculations are listed in Table 2. It is noted that the Reynolds number and momentum thickness used in our calculations are closer to the experiments.

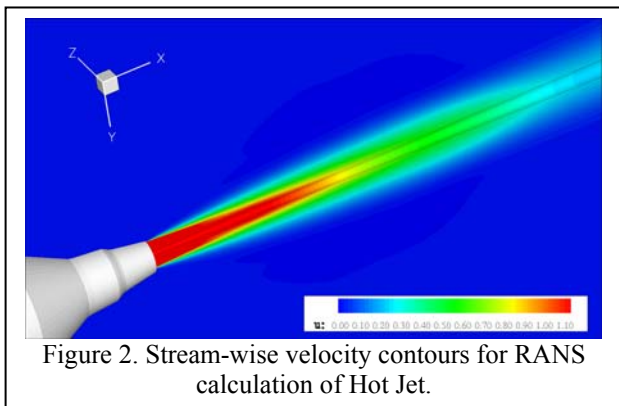


Figure 2. Stream-wise velocity contours for RANS calculation of Hot Jet.

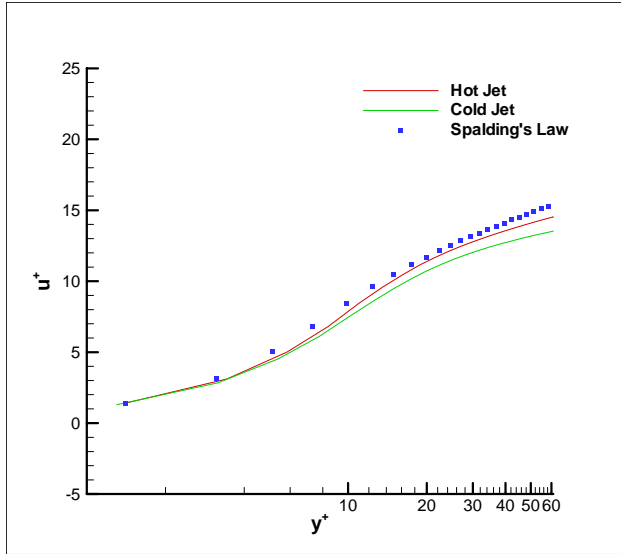


Figure 3(a). Wall-unit normalized velocity at the nozzle exit plane.

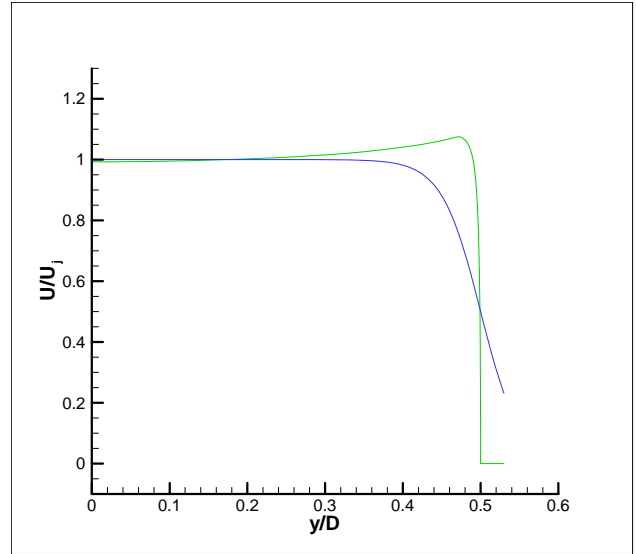
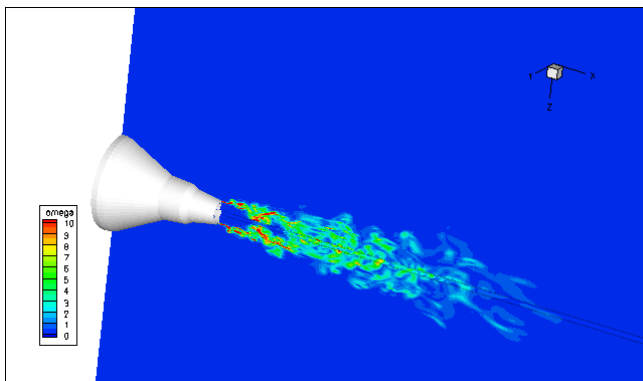


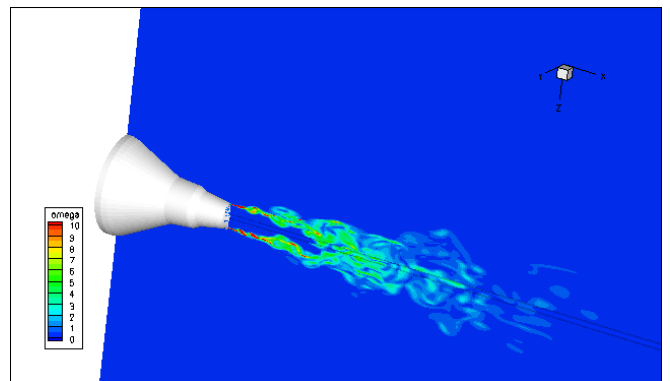
Figure 3(b). Stream-wise velocity profile at the nozzle exit plane (green line: RANS calculation; blue line: artificially-imposed inflow by Bogey et al.³).

Table 2. Jet Parameters for the LES Simulations.

		Ma	Re	Tj/T	θ
Set Point 7	Current	0.9	2×10^5	0.86	0.00181
	Bodony & Lele	0.9	8.8×10^4	0.86	0.045
	Bogey & Bailly	0.9	6.5×10^4	1.00	0.025
	Exp.	0.9	1.5×10^6	0.86	
Set Point 46	Current	0.9	2×10^5	2.7	0.00183
	Bodony & Lele	0.9	1.3×10^4	2.7	0.045
	Exp.	0.9	2×10^5	2.7	



(a) Compact Scheme



(b) MUSCL-Roe Scheme

Figure 4. Vorticity contours from the LES simulation of hot jet, using a) the compact scheme, b) the MUSCL-Roe scheme.

Various numerical schemes with different orders of accuracy have been tested in our LES calculations, including the compact schemes and the MUSCL-Roe, for which early-time ($t \approx 60$) results of vorticity contours normalized by D_j/U_j the figure demonstrates that both numerical schemes are able to successfully capture the initial vortex-rollup process of the mixing layers and the turbulent structures downstream. It is also noted that the compact scheme

resolves more detailed vorticity structures than the MUSCL scheme. However, the compact scheme requires a much finer time step size ($\delta t = 0.001$) compared to the MUSCL-Roe scheme ($\delta t = 0.01$), and we have not been able to carry out simulations to establish an overall relative efficiency of the compact scheme. Therefore, the results in this paper have been obtained from long-time calculations with the MUSCL-Roe scheme.

Time-averaged flow quantities in Figures 5 through 7 are obtained from the quasi-steady flow solutions from $t = 156$ to $t = 258.4$. Figure 5 presents the centerline mean velocity and stream-wise turbulent intensity profiles, which are compared with the experimental data³² and the LES results from Bodony and Lele³¹ for both Set Point 7 (SP7) and Set Point 46 (SP46). Our LES results compare well with the results of Bodony and Lele,³¹ both of which predict a shorter potential length than the experimental data. Bodony and Lele³¹ attribute this discrepancy to the numerically-generated large-scale organized structures in their simulations. They argued that the organized motion of the jet column instabilities is more efficient in extracting energy from the jet than the smaller scale shear layer is. They also pointed out that the numerically-imposed oscillations at the inflow boundary are different from the conditions of the experiments. In our case, numerical perturbations are not imposed at the inflow boundary, but the turbulence intensity level at the nozzle exit is somewhat smaller than in the experiments (Fig. 5(b), 5(d)). We suspect that the lack of turbulence at the nozzle exit could generate artificially-organized flow structures that cause a faster decay of the axial velocity.

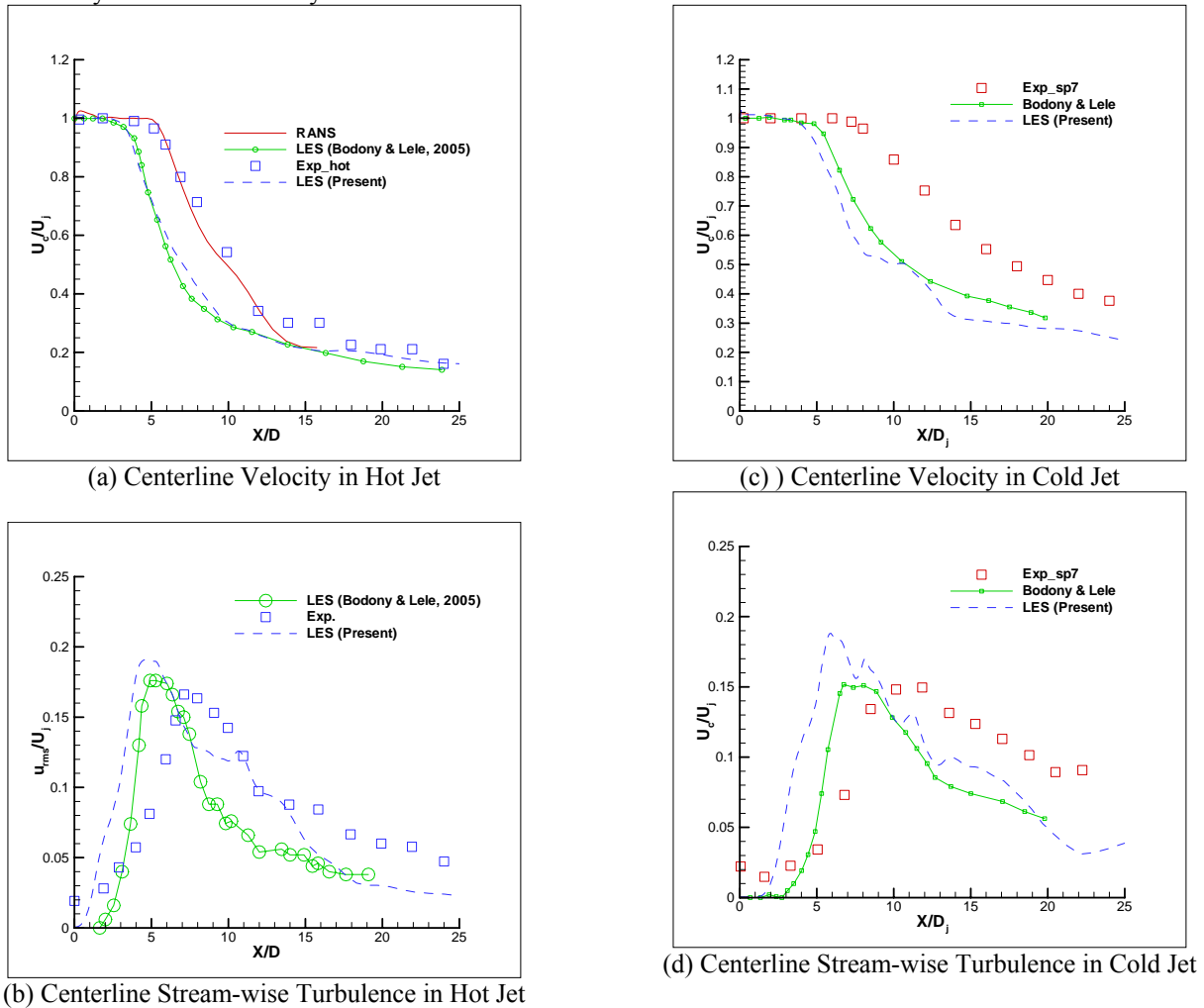


Figure 5. Mean centerline axial velocity and stream-wise turbulent intensity in original coordinates.

As in Bodony & Lele¹⁸ and Bridges & Wernet¹⁹, we use the Witze correlation²⁰ to rescale the numerical data, which is then compared with the experimental data (Figure 6). The Witze correlation used here has the formula as

$$\hat{x} = \kappa(x - x_c) \cdot (\rho_\infty / \rho_j)^{1/2},$$

where $\kappa = 0.08(1 - 0.16M_j)(\rho_\infty / \rho_j)^{-0.22}$, and x_c is a shift factor that accounts for the difference in the potential length.

Figure 6 shows the mean centerline velocity and stream-wise turbulent intensity profiles in re-scaled coordinates. It shows that the present LES results compare well with those from Bodony & Lele.¹⁸

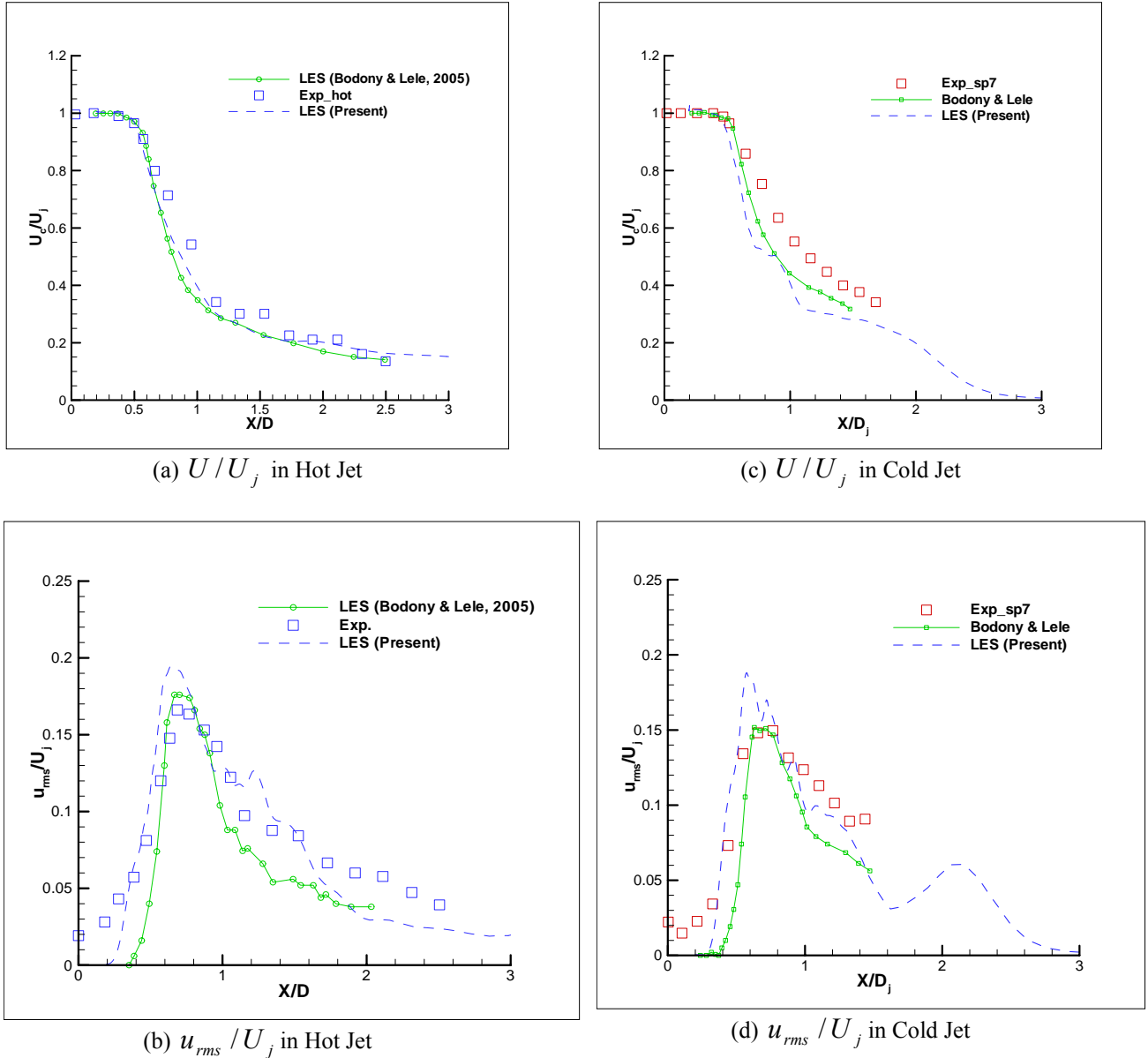


Figure 6. Centerline axial mean velocity and stream-wise turbulent intensity in original coordinates.

Figure 7 compares the radial profiles of mean velocity and stream-wise turbulent intensity of hot jet with experiments²¹ at the cross-section of $x/x_L = 0.5566$, where x_L is the length of the potential core. It can be seen that the agreement with the experimental data is excellent.

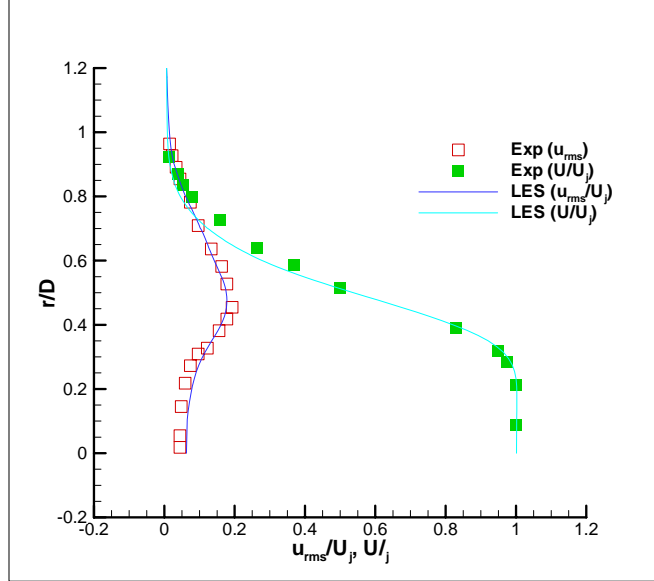


Figure 7. Radial profiles of mean velocity and stream-wise turbulent intensity of hot jet at cross-section of $x/x_L = 0.5566$.

It can be concluded that the near-field velocity and turbulence results predicted by the current LES compare well with the LES by Bodony and Lele.¹⁸ However, both the current LES and the simulation by Bodony and Lele¹⁸ under-predict the potential core lengths, which may affect the computed sound generation. The following subsection describes the comparison of the near-field and far-field prediction from LES with the data of experiments.

Near-Field Pressure Analysis

Comparisons of computed and measured near-field pressure are made in terms of the cross-spectral density $R_m(x_1, x_2, \omega)$ (Eq. 13). As discussed in Reba et al.^{[10][11]} this quantity can be viewed as the large scale turbulence noise source. The experimental data presented herein was acquired using a 78-microphone hydrodynamic array in the NASA Glenn Small Hot Jet Acoustic Rig (SHJAR). The array was designed by Suzuki and Colonius^[26] for purposes of instability wave detection, and consisted of 13 rings spaced axially by .625 jet diameters, each with 6 microphones equally spaced around the azimuth. The ring diameter increased with downstream distance to roughly follow the jet spreading. The microphone distance from the jet centerline ranged from 1 to 2.5 jet diameters.

Figures 8 and 9 show comparisons for the hot jet. In Figure 8, LES results for the real part of $R_m(x_1, x_2, \omega)$ (top row) are compared to the experimental data (bottom row) at three frequencies ($S_t=0.156$, $S_t=0.313$, $S_t=0.391$) for azimuthal mode $m = 0$. It is apparent that spatial de-correlation of the large-scale turbulence, including phase behavior, is captured reasonably well, although the simulated turbulence de-correlates more rapidly with spatial separation. Also, the peak of $R_m(x_1, x_2, \omega)$ in the LES is somewhat upstream of the measured peak, consistent with the shorter potential core in the simulation. Figure 9 compares the near-field pressure spectra along the array (i.e. R_m for $x_1=x_2$). The LES generally captures evolution of the spectral shape with downstream distance, and correctly predicts the peak Strouhal number. It must be pointed out that in Figure 9, the numerical data have been shifted by -10dB to match the experimental data.

Figures 10 and 11 show analogous results for the cold jet. Figure 10 shows the real part of $R_m(x_1, x_2, \omega)$ from the LES (top row) and from the experiment (bottom row) at three frequencies ($S_t=0.0781$, $S_t=0.195$, $S_t=0.312$) for azimuthal mode $m = 0$. Figure 11 compares the near-field pressure spectra along the array (i.e. R_m for $x_1=x_2$), where the simulation results have been shifted by -10 dB. As in the hot case, the LES captures evolution of the spectral shape with downstream distance, correctly predicts the peak Strouhal number, and reasonably captures the multi-point statistics of the large scale turbulence. However, in both the hot and cold cases, the predicted turbulence structures appear to be significantly more energetic.

Far-Field Sound Prediction

The far-field acoustics is obtained by the Ffowes-Williams/Hawkings projection method in Eqn. (16). To assess the numerical errors introduced by the far-field approximations in Eqn. (16), and to validate the numerical

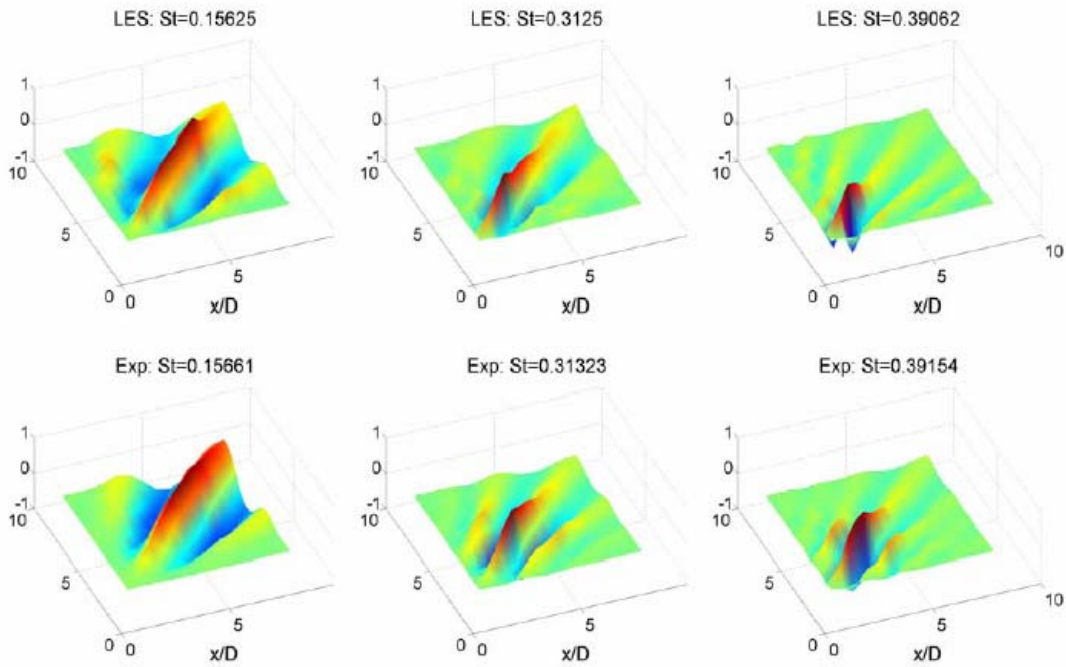


Figure 8. Real part of $R_m(x_1, x_2)$ for mode $m = 0$ (hot jet).

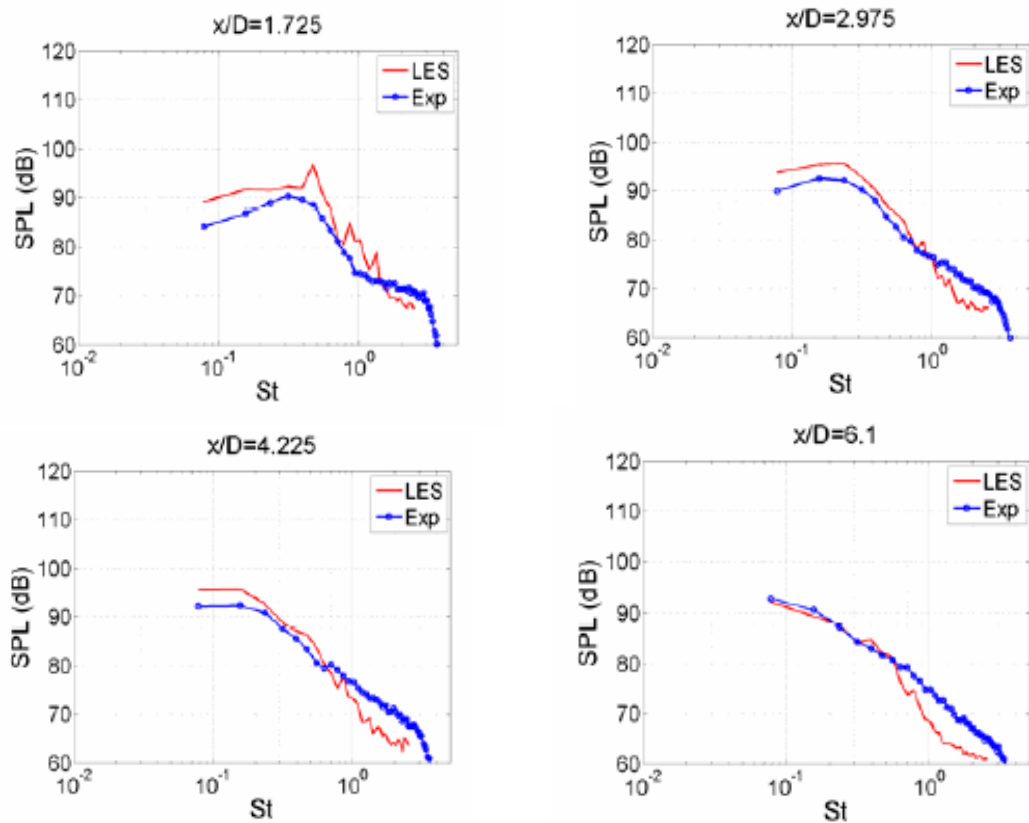


Figure 9. Computed (corrected by -10dB) and measured near-field SPL spectra ($m=0$) at different downstream locations for hot jet (a: $x/D=1.725$, $r/D=1.125$; b: $x/D=2.975$, $r/D=1.375$; c: $x/D=4.225$, $r/D=1.625$; d: $x/D=6.1$, $r/D=2.0$).

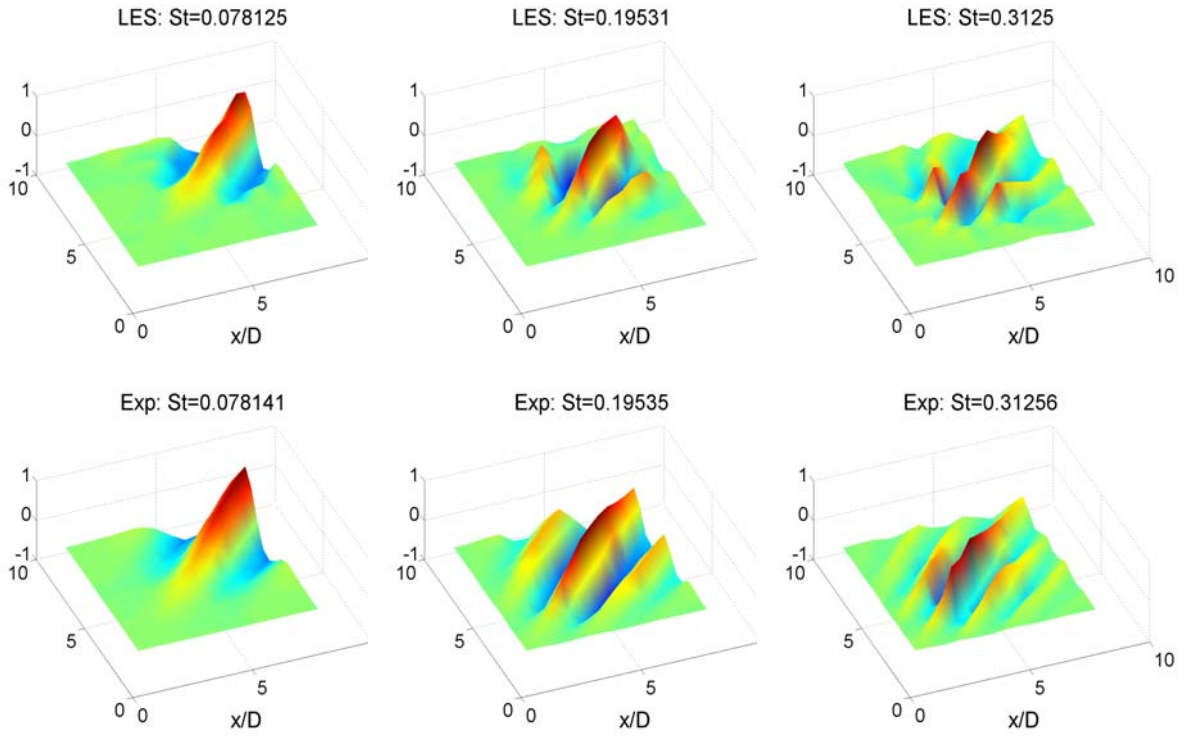


Figure 10. Real part of $R_m(x_1, x_2)$ for mode $m = 0$ (cold jet).

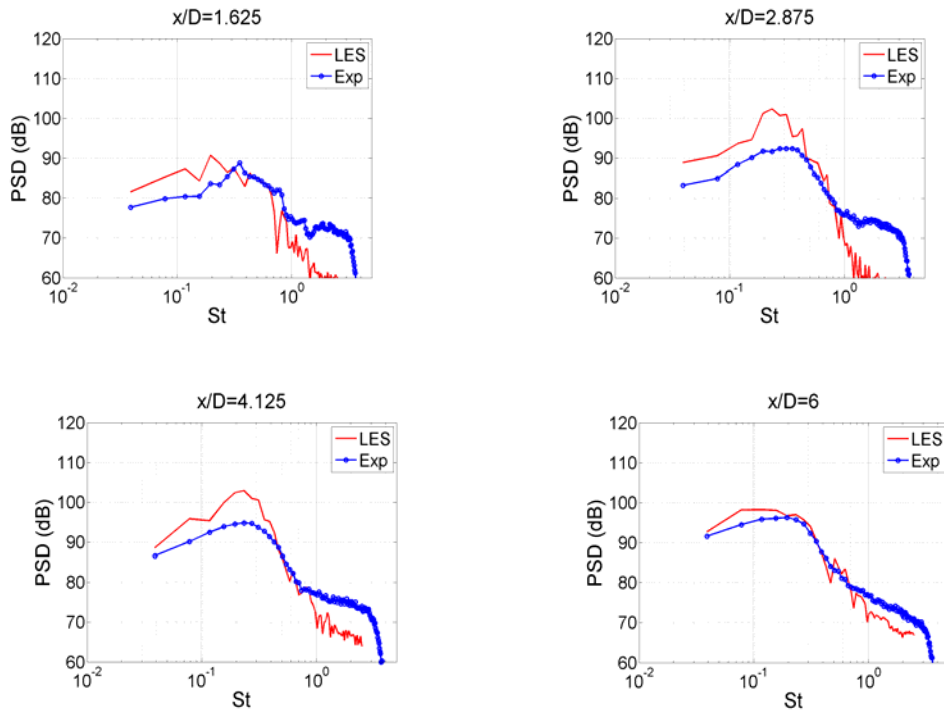


Figure 11. Computed (corrected by -10dB) and measured near-field SPL spectra ($m=0$) at different downstream locations for cold jet (a: $x/D=1.625$, $r/D=1.125$; b: $x/D=2.875$, $r/D=1.375$; c: $x/D=4.125$, $r/D=1.625$; d: $x/D=6.0$, $r/D=2.0$).

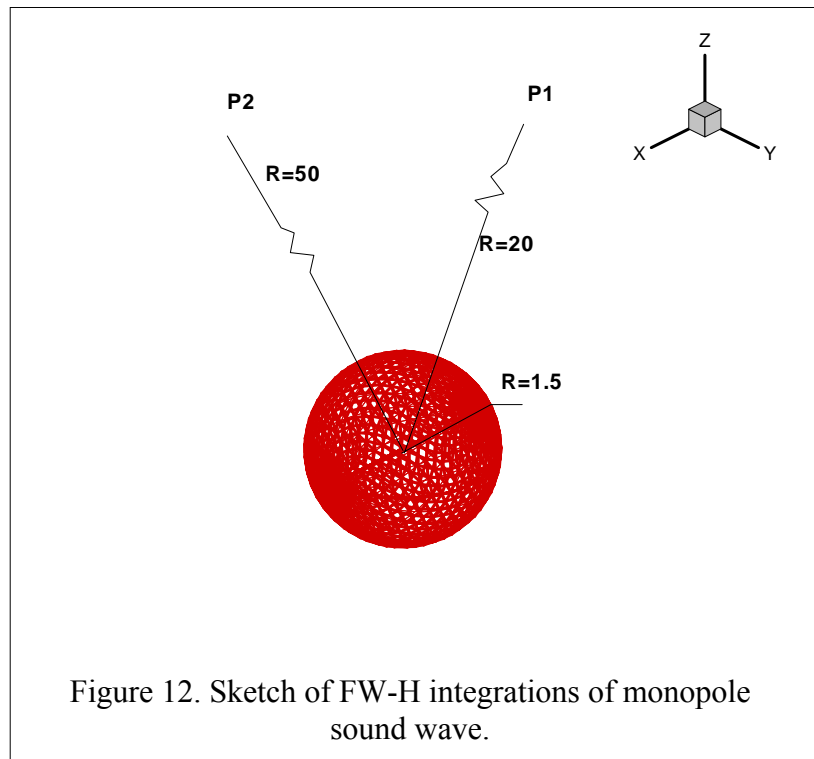
procedure, a monopole sound propagating wave is tested first. The monopole sound wave satisfies the equation

$$\frac{\partial^2 \Phi}{\partial t^2} = c^2 \nabla^2 \Phi, \quad (18)$$

where Φ is the potential function. The pressure of the sound wave has the form as

$$p = -\rho_0 \frac{\partial \Phi}{\partial t} = \frac{1}{R} \sin\left(\omega\left(t - \frac{R}{c_0}\right)\right),$$

where all variables are non-dimensional and R is the distance from the monopole sound source as shown in Figure 12. The Ffowcs-Williams/Hawkings integration surface is located at the surface of $R=1.5$. Figure 13 shows the predicted sound pressures at P1 ($R=20$) and P2 ($R=50$), compared t with the analytical solutions. Excellent agreement can be observed, showing that the present FWH approach is potentially very accurate.



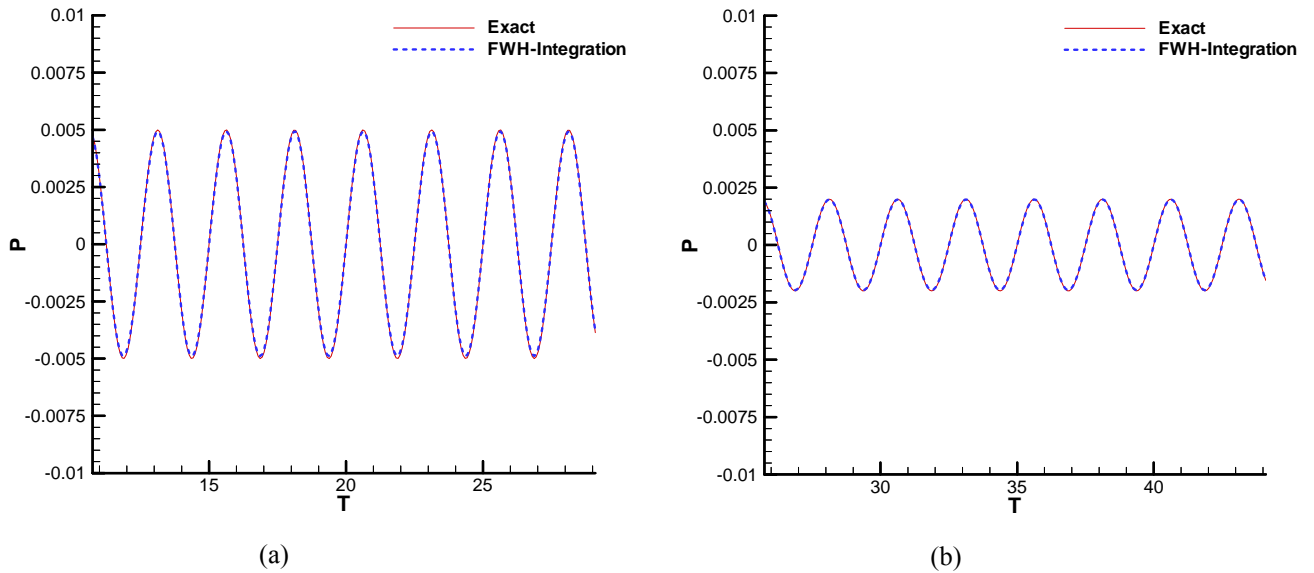


Figure 13. Far-field sound pressure obtained with the FW-H integration methods: (a) $R=20$; (b) $R=50$.

We then use the developed FWH procedure to project the near-field results to the far-field OASPL for both hot and cold jets.

Various locations of the FW-H surfaces are tested, which provide a guide on whether the quadrupole contribution from the Lighthill source is negligible (Figure 14). The near-field microphone locations used in the experiments are also shown in Figure 14. W_i denotes various span-wise widths and L_i , downstream locations.

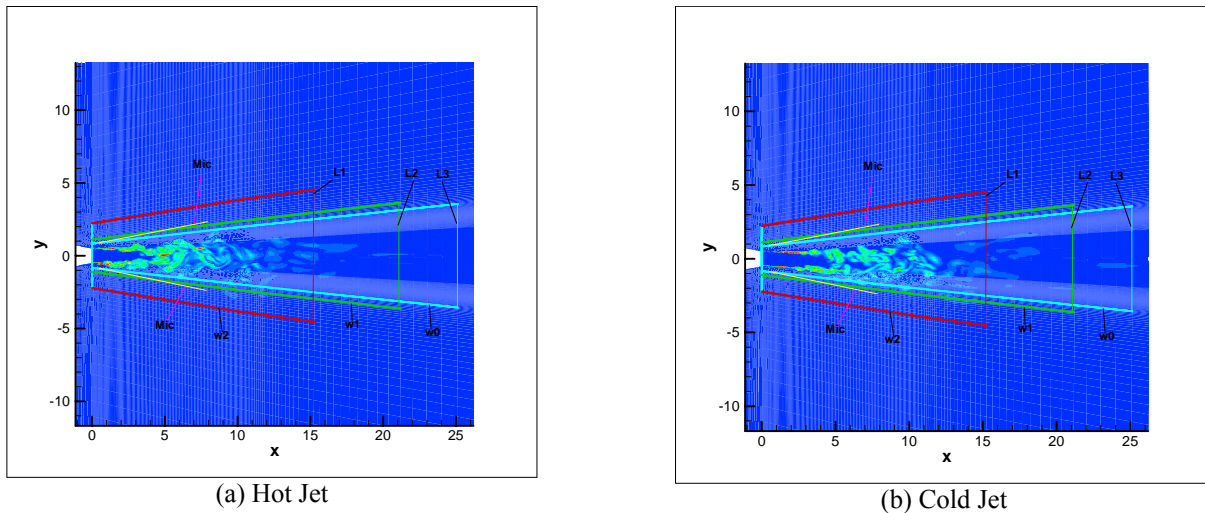


Figure 14. Various Fwocs-Williams/Hawkings Integration Surfaces.

Figure 15 shows the directivity of far-field sound OASPL obtained with the FWH method. It can be seen that the selected locations of the integration surface produce almost a converged solution in the mid-range of the angles, but show significant variance in smaller angles where large-scale mixing noise dominates. Compared with the experiments, the directivity profile has been correctly predicted by the current LES. It is observed that the shift of peak OASPL to larger angles when temperature ratio is increased is correctly predicted. The wider large-amplitude OASPL zones in the hot jet have also been captured by the LES. However, an over-prediction of the sound level has been observed for both the hot jet (10 dB) and cold jet (3 dB), compared to the 10 dB difference in near-field results. Although we are aware of several LES simulations that have reported similar over-predictions (for example, see Muller et al.²⁵ and the results of Bodony and Lele in Figure 15), further work is needed to address this issue.

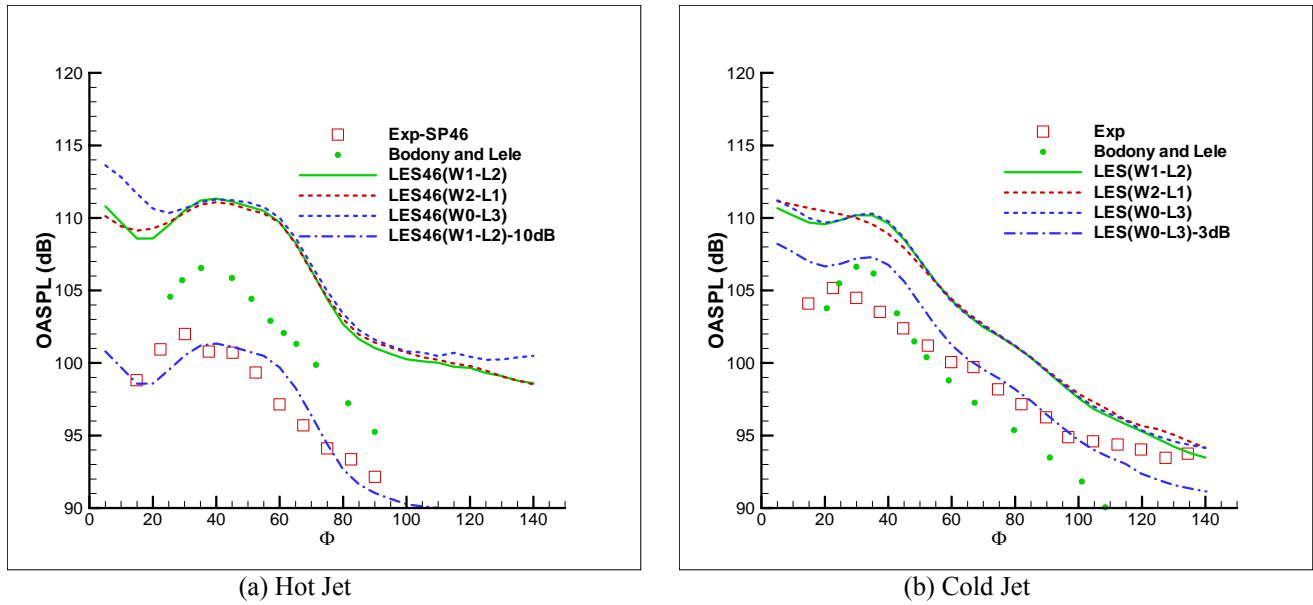


Figure 15. The OASPL profile from the FWH calculations as a function of the directivity angle.

V. Concluding Remarks

A few conclusions can be drawn from the present work. The simulation of the near-field flow uses an overset, high/low-order hybrid RANS/LES procedure, with the inclusion of the nozzle into the model. The far-field noise is obtained by the Ffowcs-Williams/Hawkings (FWH) projection method. Both the near-field hydrodynamic pressure and far-field acoustic pressure are compared with experimental data. However, while far-field results (experiments, simulations) for the chosen Tanna set points are common place, only one source of data (experiments) was found for validating the near-field solutions. Our simulation procedure appears to capture trends observed in the experiments. The fact that the near-field pressure levels require re-scaling by 10 dB in order to achieve quantitative agreement (for both the cold and hot jets) is somewhat unsettling, although similar observations have been reported by others²⁵. Also of concern is the different re-scaling requirements in the acoustic far-field for the cold and hot jets (3dB and 10 dB, respectively), while 10 dB corrections were required in the near field for both cases. This issue is being actively investigated by our group.

Acknowledgements

This work is supported by the US NAVY SBIR Phase II contract N68335-07-C-0017, with Dr. John Spyropoulos as Technical Monitor.

REFERENCES

- ¹Lele, S.K. 1992 "Compact finite difference schemes with spectral-like resolution," *J. Comp. Phys.* 103, pp. 16-42.
- ²Uzun, A. and Hussaini, Y. "High frequency noise generation in the near-nozzle region of a jet," 12th AIAA/CEAS Aeroacoustics Conference, Cambridge, Massachusetts, AIAA paper 2006-2499.
- ³Bogey, C., Bailly, C. and Juve, D. "Noise generation of a high subsonic, moderate Reynolds number jet using a compressible LES," *Theor. Comp. Fluid Dyn.* Vol 16, 2003, pp.273-297.
- ⁴Lew, P., Blaisdell, G.A., and Lyrantzis, A.S. (2005) "Recent progress of hot jet aeroacoustics using 3-D large-eddy simulation," AIAA-2005-3084.
- ⁵Bodony, D.J. and Lele, S.K. (2006) "A review of the current status of jet noise predictions using large-eddy simulation," 44th AIAA Aerospace Sciences Meeting and Exhibit, AIAA paper 2006-486.
- ⁶Bogey, C. and Bailly, C., "Contributions of computational aeroacoustics to jet noise research and prediction." *Int. J. Computational Fluid Dynamics*, Vol. 18 (6), pp. 481-491, 2004.
- ⁷Tam, C.K.W. and Auriant, L. (1999) "Jet mixing noise from fine-scale turbulence", *AIAA J.* 37(2), 145-153.

- ⁸Tam, C.K.W. and Ganesan, A. (2003) "A modified k-e turbulence model for calculating the mean flow and noise of hot jets," AIAA Paper 2003-1064.
- ⁹Tam, C.K.W., Pastouchenko, N.N. and Viswanathan, K. (2004) "Fine scale turbulence noise from hot jets," AIAA 2004-362.
- ¹⁰Reba, R, Narayanan, S., Colonius, T., and Suzuki, T. "Modeling jet noise from organized structures using near-field hydrodynamic pressure," 11th AIAA/CEAS Aeroacoustics Conference, Monterey, California, AIAA paper 2005-3093
- ¹¹Reba, R, Narayanan, S., Colonius, T., and Dunlop, M. J. "A study of the role of organized structures in jet noise generation," 9th AIAA/CEAS Aeroacoustics Conference, Hilton Head, South Carolina, AIAA paper 2003-3314
- ¹²Shu, C.-W., 1997, "Essentially Non-Oscillatory and Weighted Essentially Non-Oscillatory Schemes for Hyperbolic Conservation Laws," NASA CR-97-206253, ICASE Rep. No. 97-65.
- ¹³Gaitonde, D. and Visbal, M.R., "High-Order Schemes for Navier-Stokes Equations: Algorithm and Implementation into FDL3DI", Technical Report # AFRL-VA-WP-TR-1998-3060, Air Force Research Laboratory, Wright-Patterson AFB, OH (1998).
- ¹⁴Ladeinde, F., Cai, X.C., Alabi, K., & Safta, C. "The First High-Order CFD Simulation of Aircraft: Challenges and Opportunities," AIAA 2006-1526, Reno, NV, January 2006
- ¹⁵P.J. Morris, F. Farassat, "Acoustic analogy and alternative theories for jet noise prediction," AIAA J. 40 (2002) 671-680.
- ¹⁶M.L. Shur, P.R. Spalart, M. Strelets, Further steps in LES-Based noise prediction for complex jets. AIAA Paper-2006-485.
- ¹⁷H.K. Tanna, "An experimental study of jet noise, part II: shock associated noise." J. of sound and vibration (1977), 50(3):429-444.
- ¹⁸Bodony, D.J. and Lele, S., "On using large eddy simulation for the prediction of noise from cold and heated turbulent jets," Physics of Fluids 17, 2005.
- ¹⁹Bridges, J. and Wernet, M.P., "Measurements of the aero-acoustic sound source in hot jets," AIAA-2003-3130.
- ²⁰Witze, P.O, "Centerline velocity decay of compressible free jets," AIAA J. 12, 417(1974).
- ²¹Panda J. et al., "Effect of heating on turbulent density fluctuations and noise generation from high-speed jets," NASA/TM-2004-213126.
- ²²Cai, X. and Ladeinde, F., "Performance of WENO scheme in generalized curvilinear coordinate systems," Submitted to AIAA Reno Conference.
- ²³Cai, X., Ladeinde, F. and Alabi, K., "Towards predicting supersonic, hot jet noise", AIAA 2007-0826.
- ²⁴Cai, X. and Ladeinde, F., "A hybrid LES/RANS calculation of subsonic, supersonic hot jet noise", Proceedings of IGTI, GT 2007-28117.
- ²⁵F.Muller, F.Vuillot, G. Rahier, G. Casalis and E. Piot, "Experimental and numerical investigation of the near-field pressure of a high subsonic hot jet," AIAA-2006-2535, 12th AIAA/CEAS Aeroacoustics Conference.
- ²⁶Takao Suzuki and Tim Colonius "Instability waves in a subsonic round jet detected using a near-field phased microphone array", Journal of Fluid Mechanics (2006) v.565 pp 197-226.